Heliyon 9 (2023) e16103

Contents lists available at ScienceDirect

Heliyon

journal homepage: www.cell.com/heliyon

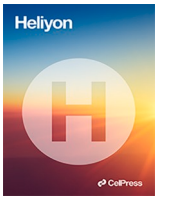

Research article

Synthesis, spectroscopic findings, SEM/EDX, DFT, and single-crystal structure of Hg/Pb/Cu–SCN complexes: *In silico* ADME/T profiling and promising antibacterial activities

Dhrubajyoti Majumdar [a,*], Jessica Elizabeth Philip [b], Amit Dubey [c,d], Aisha Tufail [c], Sourav Roy [e,**]

[a] *Department of Chemistry, Tamralipta Mahavidyalaya, Tamluk-721636, West Bengal, India*
[b] *Department of Chemistry, Alphonsa College, Palai, Kottayam, Kerala-686574, India*
[c] *Computational Chemistry and Drug Discovery Division, Quanta Calculus, Greater Noida, Uttar Pradesh, 274203, India*
[d] *Department of Pharmacology, Saveetha Dental College, and Hospital, Saveetha Institute of Medical and Technical Sciences, Chennai, Tamil Nadu, 600077, India*
[e] *Solid State and Structural Chemistry Unit, Indian Institute of Science, Bangalore 560 012, India*

ARTICLE INFO

Keywords:
Antibacterial
ADME/T
DFT
Molecular dynamics
Toxicity

ABSTRACT

This work contemplates synthesizing *M*-SCN crystal compounds (M = Hg/Pb/Cu) in the presence of respective metal salts and exogenous ancillary SCN^- ion by slowly evaporating the mixed solvent (CH_3OH + ACN). The complexes were characterized by spectroscopy, SEM/EDX, and X-ray crystallography. The Hg-Complex, Pb-Complex, and Cu-Complex crystallize in the monoclinic space group (Z = 2/4). The crystal packing fascinatingly consists of weak covalent bonding and Pb···S contacts of tetrel type bond. Here are the incredible supramolecular topographies delineated by the Hirshfeld surface and 2D fingerprint plot. The B3LYP/6–311++G (d, p) level calculations in the gas phase optimized the compound's geometry. The energy difference (Δ) between HOMO-LUMO and global reactivity parameters investigates the complex's energetic activity. MESP highlights the electrophilic/nucleophilic sites and H-bonding interactions. Molecular docking was conceded with the Gram- + ve bacterium Bacillus Subtilis (PDB ID: 6UF6) and the Gram-ve bacterium Proteus Vulgaris (PDB ID: 5HXW) to authenticate the bactericidal activity. ADME/T explains the various pharmacological properties. In addition, we studied the antibacterial activity with MIC (μg/mL) values and time-kill kinetics against *Staphylococcus aureus* (ATCC 25923) *and Bacillus subtilis* (ATCC 6635) as Gram-positive, *Pseudomonas aeruginosa* (ATCC 27853) and *Escherichia coli* (ATCC 25922) as Gram-negative bacteria.

1. Introduction

The research of metal coordination complexes with popular pseudohalides like OCN^-, SCN^-, $SeCN^-$, and N^{3-} is exciting from a structural point of view and has novel properties [1]. The motivation lies in the different coordination modes of the metal ions connected by the pseudohalides (SCN^-) (Scheme S1) [2–5]. The binding chemistry of thiocyanate-related complexes has been the

* Corresponding author.
** Corresponding author.
E-mail addresses: dmajumdar30@gmail.com (D. Majumdar), souravscott@gmail.com (S. Roy).

https://doi.org/10.1016/j.heliyon.2023.e16103
Received 30 January 2023; Received in revised form 1 May 2023; Accepted 5 May 2023
Available online 13 May 2023

subject of several reviews [6]. The spacer is arranged linearly with three different atoms and coordinates with selected metal ions in terminal and bridging modes, creating versatile structural bridging motifs of complexes. To date, different bridging modes of SCN^- have been identified in the branch of metal coordination chemistry (Scheme S1) [1,7,8]. Hence, synthesizing unique metal complexes in the presence of SCN^- co-ligands is incredible regarding supramolecular interactions [8–10] and consequently attracted much attention from synthetic inorganic chemists [11]. From another point of view, the chemistry of Hg/Pb/Cu metals is fascinating in terms of the poisoning effect and biological activities in their metal salts or complexes [12,13]. Hg and mercury compounds continue to be used in scientific research applications and the restoration of amalgam dental disease in some areas and some food manufacturing establishments. $HgCl_2$ is also used under fluorescent lighting. Notably, currently passed through mercury vapor in a fluorescent lamp produces short-wavelength UV light. It then causes the phosphor in the tube to fluoresce, making visible light [14,15]. Further, Cu is an essential dietary trace element for all living organisms. It is a critical component of the respiratory enzyme complex cytochrome *c* oxidase [16]. Concerning Pb, metal is a neurotoxin that accumulates in soft tissue and bone; it damages the nervous system, disrupts the function of biological enzymes, causes neurological disorders ranging from behavioural problems to brain damage, and affects general health, and cardiovascular and renal systems [17]. Therefore, knowledge of the poisoning effects of Hg and Pb is a matter of course for all synthetic inorganic chemists. In contrast, research is still being expanded for Hg/Pb/Cu-complexes, which are overwhelmed with SCN^- spacer [9,10,18,19]. The investigation of Hg/Cu/Pb–SCN chemistry is interested in searching for toxicity predictions via molecular dynamics simulation, supramolecular topographies, and promising antimicrobial activities. Noteworthy, crystal structures of Hg/Cu/Pb–SCN compounds are tiny explored in the literature [20–22]. Today, as part of the mandated research, synthetic researchers must rigorously observe that the quantum chemically calculated FMO, Hirshfeld surface, and MEP are becoming primary research related to steel corrosion [23,24], sensor activity [25], and chemical reactivity [26,27]. Henceforth, the breakdown of the *M*-SCN compound's exciting properties investigation like Hirshshfeld surface area, MEP, atomic/global parameters, ADME/T toxicity predictions, *in silico* molecular docking, and an antibacterial evaluation is entirely lacking in the literature. Thus, synthetic researchers develop an interest in this field. Further, the ADME/T application plays a crucial role in drug discovery development in the molecular dynamic's community. Noteworthy, ADME/T determined the pharmacokinetic and pharmacodynamic properties of the different compounds [28]. Many *in silico* models are currently being developed to predict the chemical properties of ADME/T. The simplest form of toxicity prediction is cytotoxicity, where the drug molecule severely damages cells. The compounds' mutagenicity and carcinogenicity generally predict by ADME/T study, thereby avoiding compound toxicity [28]. The present research stems from our interest in investigating *M*-SCN crystal compound coordination behaviour associated with the molecular dynamic's community.

This article vividly reported the synthesis, characterization, and single-crystal structures of Hg/Cu/Pb–SCN compounds. Quantum chemical DFT calculations explore the atomic properties and the global reactivity parameter. The HOMO-LUMO energy difference and MEP study support the compound's reactivity. Moreover, ADME/T explores the theoretical drug-like properties and toxicity profiling. *In silico* molecular docking examined the antimicrobial efficacy of the compounds. Finally, the promising antibacterial activity with MIC (μg/mL) values and time-kill kinetics were studied against the important *Staphylococcus aureus* (ATCC 25923) *and Bacillus subtilis* (ATCC 6635) as Gram-positive, *Pseudomonas aeruginosa* (ATCC 27853) and *Escherichia coli* (ATCC 25922) as Gram-negative bacterial strains. The complexes imply greater antimicrobial efficiencies over metal salts.

2. Experimental section

2.1. Starting materials

The starting research materials were of analytical grade and used as received without further purification. The research chemicals NaSCN (98%), $Pb(NO_3)_2$ (99%), $Cu(NO_3)_2$ (99.99%), and $HgCl_2$ (99.5%) were purchased from Sigma Aldrich Company, USA, and the CH_3OH solvent used was a spectroscopic grade.

2.2. Physical measurements

Elemental analyses (C, H, and N) of *M*-SCN crystal compounds were performed using a PerkinElmer 2400 CHN Elemental Analyzer. The IR spectra were obtained by recording KBr pellets (4000-400 cm^{-1}) with 16 scans at a wave number resolution of 4 cm^{-1} using a PerkinElmer Spectrum RX 1 instrument equipped with a DTGS detector (Deuterated Triglycine Sulphate). Raman spectra were recorded as solid BRUKER RFS 27 (4000-50 cm^{-1}). JEOL Model JSM6390LV investigated the SEM micrographs for the synthesized compounds. The EDX was performed on EDX OXFORD XMX N using W filament.

2.3. Computational methodology

2.3.1. Density functional theory

The *M*-SCN compounds' geometry was optimized in the gas phase using the B3LYP model owing to its strong geometry optimization capabilities and exact prediction of reaction enthalpies using the 6–311++G (d, p) basis set [29–33]. The software Avogadro was used to visualize the molecular structures. DFT studies were carried out using the Gaussian 09 [34] software package, and Gauss View 09 was used to display the outcomes. It is carried out on the complexes of Hg-Complex, Pb-Complex, and Cu-Complex using the basis set 6-31G without any geometrical restrictions. For the complexes' energetic behaviour, we calculate the HOMO-LUMO energy difference. It explains the chemical hardness, softness, electronegativity, and electrophilicity index. Hirshfeld surfaces [35–37] and two-dimensional (2D) fingerprint plots [38,39] have been calculated using Crystal Explorer software [40]. The bond lengths of

hydrogen atoms have been set to typical values. D_e and d_i are defined for each point on the Hirshfeld surface to calculate the normalized contact distance (d_{norm}) using the appropriate formula. The d_{norm} value depends on the relative values of intermolecular contacts and van der Waals separations. The Hirshfeld surface with a red-white-blue color scheme is displayed with the d_{norm} parameter. The bright red spots indicate shorter contacts. White areas represent contacts around the van der Waals separation, and blue regions, conversely, signify the absence of any close contacts.

2.3.2. Molecular docking

SBDD (structure-based drug discovery) approach analyzes molecular recognition, and it is for binding energetics, molecular interactions, and induced conformational changes. Molecular docking (MD) and structure-based virtual screening (SBVS) will also be equally important [41,42]. MD predicts how particular molecules interact with the target protein's binding sites. Here MD experiment was carried out on the Gram-positive bacterium Bacillus Subtilis (PDB ID: 6UF6) [43] and the Gram-negative bacterium Proteus Vulgaris (PDB ID: 5HXW) [44]. The Molegro Virtual Docker (MVD) docking software was used for the MD operation [45–49]. The cavity with the possible binding site for ligands in receptor structure was automatically identified using the grid-based cavity prediction. The residues near the cavity were kept to a minimum. Only the side chains' torsion angles changed during the reduction process; all other parameters, such as bond lengths and backbone atom locations, remained unchanged. The ligands' 3D structures were imported into MVD as *pdb format. The backbone was kept stiff throughout the docking simulation. The side chains of amino acids adjacent to the discovered cavity were allowed to alter in torsional angles. The softer potentials were docked with the ligands. The receptor was kept stiff at this point in its default conformation. After each ligand was docked, the side chains selected for minimization were minimized concerning the discovered pose. The conventional non-softened potentials rearranged the side chains and minimized the ligand. Since it is a significant reduction in the intricacy of the docking search, if fewer flexible torsions are set during the docking run, all flexible torsions in the ligand are set stiff during docking.

2.3.3. ADME/T and toxicity

For the proposed chemical compound that might be utilized as a medicine, it is crucial to examine ADME (Adsorption, Distribution, Metabolism, and Excretion). The website SwissADME (available at https://www.swissadme.ch) allows users to draw their desired ligand or drug molecule or include SMILES data, provides parameters such as lipophilicity (iLOGP, XLOGP3, WLOGP, MLOGP, SILICOS-IT, Log Po/w), water solubility- Log S (ESOL, Ali, SILICOS-IT), drug-likeness rules [50]. The search field entered the SMILES code of Hg-Complex, Pb-Complex, and Cu-Complex cif data. Then examined, a micro molecule is injected into human and animal models, and it is vital to forecast its toxicology to determine how tolerable it will be. A micro molecule can be virtually sketched in or examined by submitting its SMILES to Discovery Studio 2.0.

3. Experimental of antimicrobial

3.1. Bacterial cultures

The antibacterial efficacy of Hg/Pb/Cu-Complexes and the associated metal salts ($HgCl_2$/$Pb(NO_3)_2$/$Cu(NO_3)_2$/NaSCN) were evaluated against *Staphylococcus aureus* (ATCC 25923) and *Bacillus subtilis* (ATCC 6635) as Gram-positive bacteria. Also, as *Pseudomonas aeruginosa* (ATCC 27853) and *Escherichia coli* (ATCC 25922) as Gram-negative bacteria. For the study, we used the Agar Well Diffusion method to determine the quality of the samples. The MIC values were determined using serial dilutions in the liquid broth method. All ATCC strains were obtained from the American Type Culture Collection in Manassas, VA, USA, and the media used in the study were purchased from Himedia in India.

3.1.1. Maintenance of cultures

All bacterial cultures were preserved in 50% glycerol at −70 °C (vol/vol; Himedia, Mumbai, India) and maintained on Trypticase Soy Agar (TSA; Difco Laboratories, Detroit, Mich USA) were held on Sabouraud Dextrose Agar (SDA; Himedia).

3.1.2. Antimicrobial study: Agar Well Diffusion

The complexes and the metal salts were inoculated with *Staphylococcus aureus*, *Bacillus subtilis, Pseudomonas aeruginosa*, and *Escherichia coli* incubated at 37 °C. The microbial turbidity was adjusted to equivalent to a 0.5 McFarland turbidity standard. After that, Mueller-Hinton agar plates (Merck, 105437) were swabbed uniformly with the standardized inoculums. Once the surfaces of the agar plates were dried, 6 mm three wells were bored using a sterile cork-borer about 2 cm apart. The bottom of each well was coated with sterilized Mueller-Hinton agar at 45 °C. To prepare for testing each microorganism, the sample was dissolved in DMSO and added to a well. It was then left to diffuse at room temperature for 2 h. Then, DMSO as negative control (C) was loaded into the second and third wells. All the plates were incubated face upwards among bacterial cultures at 37 °C for 24–48 h. The diameter of the inhibition zones was evaluated using a microscope scale, and six replications were maintained for each plate [51,52]. We analyzed the antibacterial experimental data through the statistical software Origin Pro 8.5 using the analysis of variance (ANOVA) method. We employed Tukey's studentized test to differentiate the mean differences, with a 1% probability level.

3.1.3. Agar dilution method: determination of MIC

The agar dilution method is a process that utilizes various concentrations of antimicrobial agents in a molten agar medium. This is done through serial two-fold dilutions and injecting a specific amount of microbial sample onto an agar plate. The lowest concentration

of the antimicrobial agent that completely inhibits growth under suitable incubation conditions [51,52] is recorded as the MIC endpoint. This technique is well-suited for testing bacterial susceptibility.

3.1.4. Time-kill kinetic

We conducted time-kill kinetics studies on the newly synthesized compound to test its effectiveness against all types of microbes. In this experiment, an overnight culture of the isolates was used up 1 mL of 10^6 CFU mL^{-1} of each culture. It was inoculated in sterilized nutrient broth media containing 25 $mgmL^{-1}$ of the compounds. The experiment was conducted for 13 h in a shaker at 30 °C, preparing control for each microorganism without having the test compound. At regular 1-h intervals, the CFU count was measured. In this experiment, 1 mL of each culture was spread on nutrient agar plates between 0 and 13 h. The plates were then incubated at 30 °C for 24 h. The resulting CFU count was used to create a graph [53].

4. X-ray crystallography

We grew the *M*–SCN–type crystal complex at room temperature by slowly evaporating a mixed solvent atmosphere of methanol and acetonitrile (ACN). Afterward, we selected 3–4 high-quality crystal samples through microscopic observation for SCXRD purposes. Bruker CCD [54] diffractometer processed the crystal data using Mo Kα radiation (λ = 0.71073 Å) at room temperature (298*K*). To collect data, we utilized various crystallographic programs. *SMART* was responsible for gathering information frames, indexing reflections, and determining lattice parameters. *SAINT* [55] combined reflection intensity and scaling, while *SADAB* [56] handled absorption correction. *SHELXTL* was used for space group and structure determination and least-squares determination refinements on F^2. The crystal structure was solved by full-matrix least-squares methods against F^2 using *SHELXL*-2014 [57] and *Olex-2* [58]. The refinement of all non-H atoms included anisotropic shift parameters, while the H positions remained constant at their calculated positions. Table 1 provides a comprehensive summary of the crystallographic information and parameters for the structure refinement.

5. Synthesis of *M*-SCN complexes

We synthesize *M*-SCN crystal complexes as per the experimental protocol described below. Although the *M*-SCN complexes synthesis has already been published in the literature [20–22], we still use an entirely new method.

Synthesis for *M*-SCN (M = Pb/Cu): In a 100 mL round bottom flask, we mixed, after stirring for 10 min, salts like $Pb(NO_3)_2$ (0.331 g, 1 mmol) and $Cu(NO_3)_2$ (0.187 g, 1 mmol) in 50 mL CH_3OH + ACN (acetonitrile) combined solvent medium. The mixture refluxed for 2 h, in the presence of NaSCN (0.081 g, 1 mmol), cooled, and continued stirring for about 1 h. The solution was filtered and refrigerated for crystallization by slow evaporation at room temperature. After 7–8 days, block-sized, light yellow (for Pb) and light green (for Cu) developed single crystals, suitable for X-ray diffraction study. Crystals were isolated by filtration, washed with dry ether, and air-dried. Yield: 71%, Anal. Calc. for $C_2N_2PbS_2$: C, 7.43; N, 8.66. Pb, 64.08, S, 19.83 Found: C, 7.38; N, 8.45, Pb, 64.04, S, 19.51%. Anal. Calc. for $C_2N_2CuS_2$: C, 13.37; N, 15.59. Cu, 35.36, S, 35.69 Found: C, 13.33; N, 15.62, Cu, 35.31, S, 35.61%. FT-IR (KBr cm^{-1}) bands: ν(SCN), 2110 s, (Pb–SCN), (Cu–SCN), ν(SCN), 2114 s, NaSCN, ν(SCN), 2069 s, Raman (cm^{-1}) bands: ν(SCN), 2034 s.

Synthesis for Hg–SCN: We consider a similar method to synthesize the Hg–SCN complex, (white color), except $HgCl_2$ salts are used in place of $Pb(NO_3)_2$/$Cu(NO_3)_2$. Yield: 68%, Anal. Calc. for $C_2HgN_2S_2$: C, 7.58; H, N, 8.84, Hg, 63.39, S, 20.25 Found: C, 7.49; N, 8.51,

Table 1
Crystal data and refinement details of the complexes.

Formula	$C_2HgN_2S_2$	$C_2CuN_2S_2$	$C_2PbN_2S_2$
Formula Weight	316.75	179.71	323.36
Temperature (K)	293	293	293
Crystal System	Monoclinic	Monoclinic	Monoclinic
Space group	*C2/m*	*C2/m*	*C2/c*
a (Å)	10.890 (4)	10.890 (4)	9.691 (11)
b (Å)	4.0299 (12)	4.0299 (12)	6.556 (8)
c (Å)	6.414 (2)	6.414 (2)	8.279 (9)
α (°)	90	90	90
β (°)	95.804 (18)	95.804 (18)	92.232 (8)
γ (°)	90	90	90
Z	2	2	4
d_{cal} (g cm^{-3})	3.757	2.131	4.086
μ(mm^{-1})	28.086	4.504	32.744
F (000)	276	174	560
Total reflection	2639	2639	6964
Unique Reflections	470	430	783
Observed data [I > 2σ(I)]	429	429	746
R (int)	0.083	0.083	0.071
Goodness-of-fit on F^2	1.22	1.30	1.24
Min. and Max. Resd. Dens. [e/$Å^3$]	−3.05, 4.19	−2.47,1.79	−11.141,10.79
R1, w*R*2 (all data)	0.0522, 0.1217	0.1040,0.2698	0.0909,0.2767
R1, w*R*2 [I > 2σ(I)]	0.0520, 0.1213	0.1036, 0.2685	0.0887, 0.2742

Hg, 63.01, S, 20.21%. FT-IR (KBr cm^{-1}) bands: ν(SCN), 2109 s, NaSCN, ν(SCN), 2069 s, Raman (cm^{-1}) bands: ν(SCN), 2034 s.

6. Results and discussion

6.1. Synthetic perception

Based on previous literature [20–22], we synthesized the *M*-SCN crystal complexes using a modified and unique method. As shown in Scheme 1, our synthetic route yielded satisfactory results using *in situ* self-assembly method where $Pb(NO_3)_2$, $Cu(NO_3)_2$, and $HgCl_2$ were used as metal precursors in the presence of NaSCN in a 1:1:1 M ratio. Herein single crystals were grown with diffractive quality in contact with the mixed solvent (CH_3OH + ACN). The synthesized air and moisture-resistant compounds are characterized by elemental, IR/Raman spectroscopy, SEM/EDX, and X-ray crystallography. However, since little information about the *M*-SCN (M = Hg/Pb/Cu) crystal structures has been published in the literature [20–22], coordination chemistry researchers show potential interest concerning the compounds. Therefore, the necessity of extensive research concerning *M*-SCN compounds has yet to come to the front of global researchers. Our research group focuses on extensive research *in silico molecular dynamics*, global parameters, DFT, molecular docking, ADMET, toxicity predictions, time-kill kinetics, and antibacterial activity. Besides, we are also confirming the supramolecular interactions with tetrel-type bonding present in the Pb–SCN compound. We ensure that the investigation covered like this is wholly unveiled in the literature.

7. Spectroscopic characterization

Besides routine elemental analysis, we examined the presence of SCN^- co-ligand in the *M*-SCN crystal complexes through FT-IR and Raman spectra (Fig. S1-Fig. S2). These two spectroscopic studies deal with the vibration of the molecules. Each functional group has a discrete vibrational energy that identifies a particular molecule by combining all the functional groups. Our synthesized *M*-SCN compounds, SCN^- stretching vibration, were observed in 2109–2114 cm^{-1} [8–11]. We have also compared the IR of *M*-SCN compounds with SCN^- in Sodium thiocyanate. Here the characteristic bands (2069 cm^{-1}) confirm that SCN^- the spacer is linked with Hg/Pb/Cu metal ions. Further, the standard Raman bands near 2034 cm^{-1} agree that the thiocyanate anion bonded with the Hg/Pb/Cu metal ions.

7.1. EDX-SEM analysis

In addition to identifying the essential elements present, we conducted an EDX analysis to determine the presence of important metals and elements in the newly synthesized compounds. This type of analysis is becoming increasingly crucial in coordination chemistry, particularly in crystallography, as it provides accurate information about the composition of the compounds being studied.

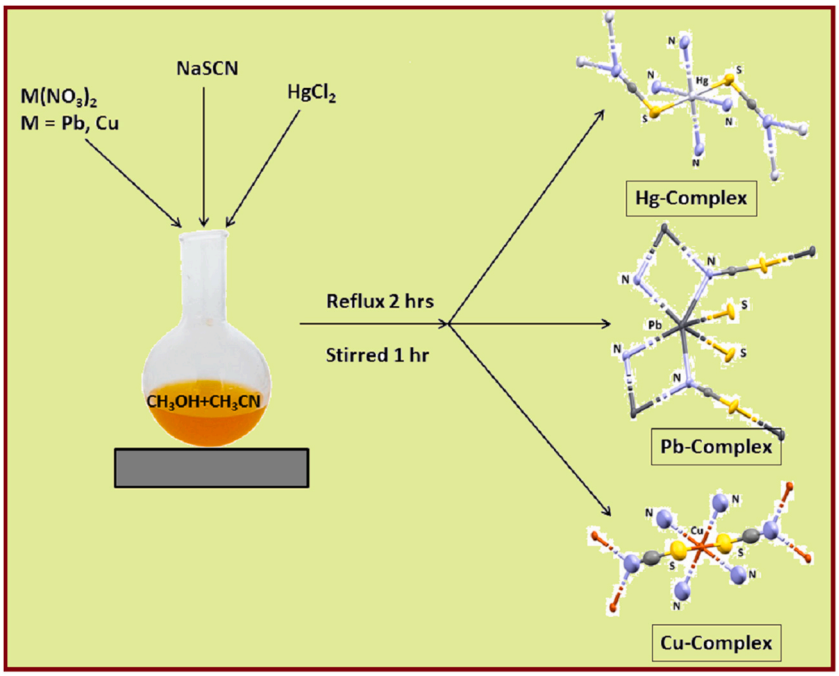

Scheme 1. Synthetic outlines for the complexes.

Through the EDX experiment, we were able to identify the main elements present in the *M*-SCN crystal compositions, which include C, O, N, and S. Additionally, we found the presence of Hg, Pb, and Cu metals in the *M*-SCN compounds as shown in Table S1 and Fig. S2A-2C. We utilized the SEM technique to study the size and shape of crystal complexes. We conducted a thorough SEM investigation on our *M*-SCN crystals (ES2-ESI3). The SEM images of the Pb–SCN compound revealed the morphology of the ice crystals. Meanwhile, the SEM profiles of the Cu–SCN/Hg–SCN compound indicated that the morphology is distributed in overlapping sheets.

8. Crystal structure description

The X-ray crystal structure determination revealed that complexes crystallize in the monoclinic space groups *C*2/*m* (Hg–SCN), *C*2/*m* (Cu–SCN), and *C*2/*c* (Pb–SCN), respectively. Details of the crystallographic data are given in Table 1, and complete crystallographic parameters are submitted in Table S2. The Hg(II) and Cu(II)-thiocyanates have comparatively similar structures where the metal centers assume octahedral geometry (Figs. 1 and 2), but the Pb(II)–SCN adopts square antiprismatic geometry (Fig. 3). In Hg–SCN and Cu–SCN, the metal centers, Hg (1) and Cu(1) are coordinated by four symmetry-related nitrogen atoms, N (1)[a], N (1)[b], N (1)[c], N (1)[d] at a distance of ~2.786 Å for Hg–SCN and ~2.698 Å for Cu–SCN from $\mu_{1,1}$ bridged thiocyanates which constitute the basal plane [the symmetry coordinates are given in Figs. 1 and 2. The axial sites are occupied by two sulphur atoms, S (1) and S (1)[e], at a distance of ~2.38 Å from two $\mu_{1,1,3}$ bridging thiocyanate completing the octahedral geometries in both complexes. The axial bonds are slightly longer in Cu–SCN (~2.39 Å) than in Hg–SCN (~2.37 Å). The *N*–Cu–N angles vary from 83° to 97° in each complex.

In complex Pb–SCN, the metal center, Pb(1) assumes square antiprismatic geometry (Fig.S2D) where four sites are occupied by four nitrogen atoms from four $\mu_{1,1}$ bridged thiocyanates at a distance of ~2.75 Å, two sites are occupied by two sulphur atoms (2.989 Å) from two thiocyanates and the other two sites are vacant. Two weak interactions have been observed in these two sites with two different sulphur atoms from two thiocyanates at 3.152 Å each, further resulting in tetrel bond formation.

8.1. Supramolecular chemistry (tetrel bond)

The crystal packing of *M*-SCN (Hg/Cu/Pb) complexes along the b axis is shown in Fig.S2E. In complexes Hg–SCN and Cu–SCN, the crystal packing mainly consists of covalent bonding, and fragile metal-carbon contacts are noticed. In contrast, in complex Pb–SCN, the crystal packing consists of covalent bonding as well as Pb···S connections referred to as tetrel type bonds [59]. These interactions are weak but significant in packing construction, as shown in Fig.S2E.

8.2. Hirshfeld surface

By conducting a Hirshfeld surface analysis, one can better understand the electronic distribution surrounding a complex's surface. This analysis can aid in analyzing the crystal packing and supramolecular interactions within a complex's solid-state structure. In this report, the crystal packing, along with the different contacts observed in three metal thiocyanates, Hg–SCN (**1**), Cu–SCN (**2**), and Pb–SCN (**3**), have been studied and analyzed. In all the complexes, Hirshfeld surfaces have been mapped over d_{norm} (−0.5 to 1.5 Å), shape index (−1.0 to 1.0 Å), and curvedness (−4.0 to 0.4 Å), as shown in Fig. 4 (extreme left). The red patches observed in d_{norm} represent interactions or contacts. In complex Pb–SCN, the red patches observed in d_{norm} are comparatively higher than the others. In comparison, complexes Hg–SCN and Cu–SCN show similar patches and interactions. Metal···N and Metal···S interactions/contacts are mainly detected. 2D fingerprint plots recognized from d_e and d_i, explain the observed contacts/interactions in the complexes (Fig. 4, extreme right). In all complexes, the metal centers are coordinated by two sulphur and four nitrogen atoms. Still, in complex Pb–SCN, two additional Pb···S contacts are observed, which resulted in two tetrel-type bonding interactions (Fig. S2E). As a result, the Pb···S (28.6%) contact in complex Pb–SCN is higher than Pb···N (22.6%) contact, whereas, in the other two complexes, Pb···N contact is higher (almost 5 times) compared to Pb···S contact.

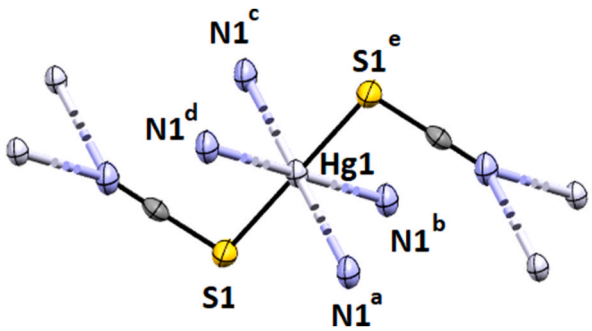

Fig. 1. Perspective view of Hg–SCN with the selective atom numbering scheme. [a] = 1/2 + x, −1/2 + y, z, [b] = 1/2 + x, 1/2 + y, z, [c] = 1/2-x, 1/2 + y, 1-z. [d] = 1/2-x, −1/2 + y, 1-z. [e] = 1-x, y, 1-z.

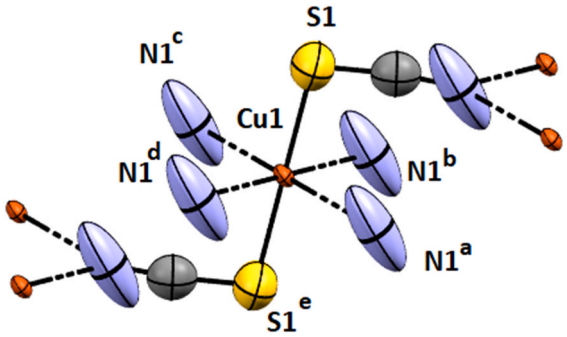

Fig. 2. Perspective view of Cu–SCN with the selective atom numbering scheme. [a] = 1/2-x, −1/2 + y, 1-z, [b] = 1/2-x, 1/2 + y, 1-z, [c] = 1/2 + x, 1/2 + y, z. [d] = 1/2 + x, −1/2 + y, z. [e] = 1-x, y, 1-z.

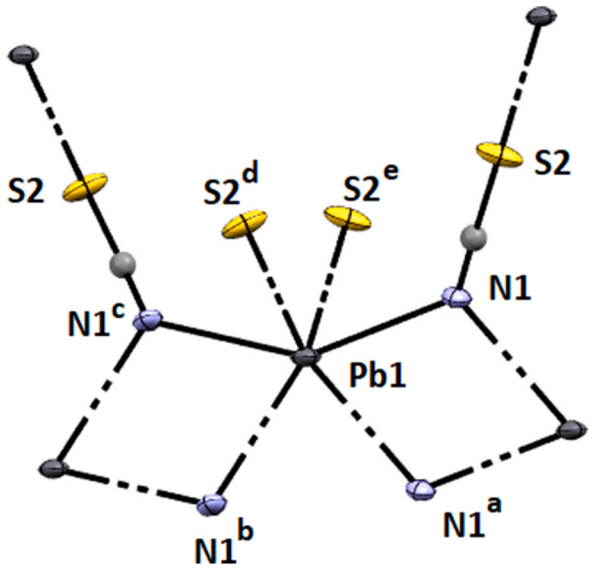

Fig. 3. Perspective view of Pb–SCN with the selective atom numbering scheme. [a] = 1-x, -y, 1-z, [b] = x, -y, −1/2 + z, [c] = 1-x, y, 1/2-z. [d] = x, 1-y, −1/2 + z. [e] = 1-x, 1-y, 1-z.

9. DFT analysis

9.1. HOMO-LUMO reactivity

The FMO approach was used to anticipate the complexes' reactivity parameters (HOMO-LUMO energy gap). Hg-Complex and Cu-Complex have HOMO orbitals with slightly lower energies than Pb-Complex (HOMO -0.1167eV and HOMO -0.14804723, respectively), indicating that Pb-Complex-valence C3's electron density distribution has a more significant potential for electron donation. The Hg-Complex energy gap (0.0002eV) is lower than the Pb-Complex and Cu-Complex energy gap (0.0034eV and 0.0039eV), which implies more chemical reactivity to the Hg-Complex (Fig. 5). Pearson's HSAB theory states that a favourable interaction between two compounds happens when both are hard or soft molecules [60,61]. As a result, the Pb-Complex molecule is thought to be hard due to its low global softness value (- 0.00197eV) and high global hardness value (S-507.4eV) as compared to the other complexes (Table 2). The reactivity descriptors, electronegativity, and electrophilicity for Hg-Complex (0.14791eV and 81.71eV) have higher values than those calculated for Pb-Complex and Cu-Complex (Table 2). Therefore, Hg-Complex is more susceptible to accepting electronic density. Other parameters are mentioned in Table 2. Remarkably, we also calculated different DFT parameters, such as bond length and angles, which are almost comparable to the *M*-SCN compounds (Table S3).

9.2. MESP investigation

The MESP is a meaningful statistic that describes the electrophilic attack sites, nucleophilic reactions, and hydrogen bonding interactions. The maps were created to analyze a molecule's structural characteristics. The significance of MESP lines shows the color

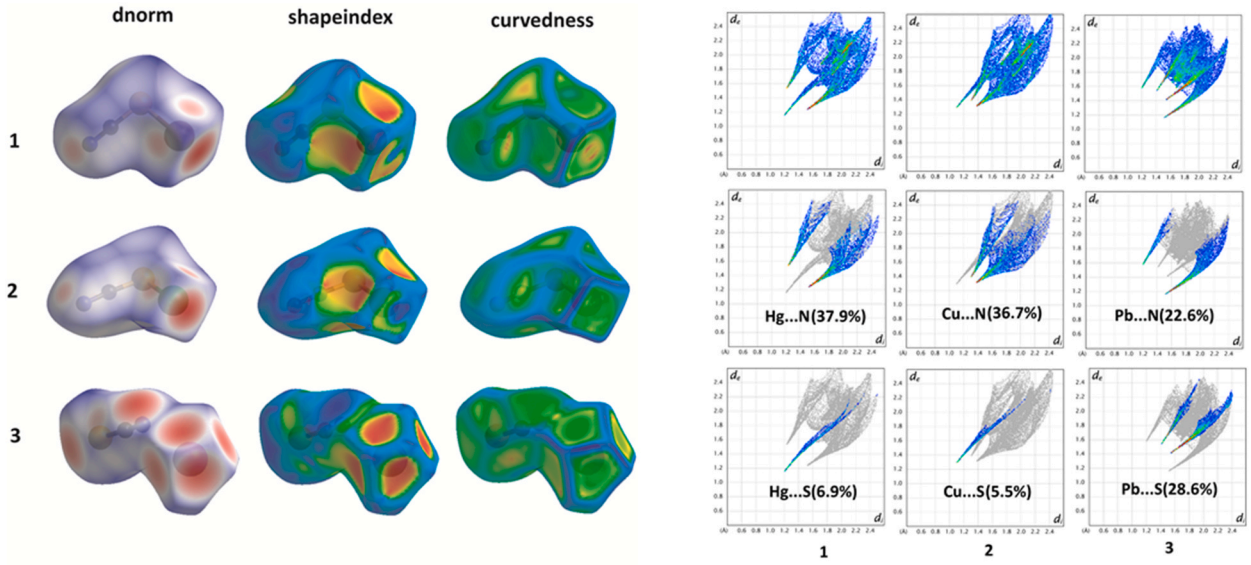

Fig. 4. HS mapped with d_{norm}, shape index, and curvedness (left), and 2D fingerprint plot disintegrated into different contacts for complexes (**1**–**3**) (right).

grading scheme's form, size, and negative, positive, and neutral electrostatic potential areas. The MESP Iso-values and color Scale shown in Table 3 and Fig. 6(a–c) shows the MESP of the complexes. The most positive electrostatic potential of the molecules is shown by the blue color-coding region (signifying a severely electron-deficient area). The red color-coding area (indicating an electron-rich part) represents the most electronegative potential. In the case of the Hg-Complex complex, the most positive electrostatic potential is located at H1, S1, S2, and S3 atoms, whereas the most electronegative potential is located at N1, N2, N3, and N4. (Fig. 6a). In the case of the Cu-Complex complex, the most positive electrostatic potential is located at H1, H3, S4, and Cu2 atoms, whereas the most electronegative potential is located at N1, N2, N3, and N4. (Fig. 6b). Interestingly, in the case of Pb-Complex, most positive electrostatic potential is located at H5, H6, H8, H13, H14, and S6 atoms, whereas most electronegative potential is located at N1, N2, N3, N4, N5, N6 and C2 (Fig. 6c).

9.3. Atomic parameters

Rigorous calculations have been made in favour of ESP, Hirshfeld, and Mulliken's atomic charges. Here DFT computed atomic charges may reveal the charge distributions of certain atoms. The Hirshfeld negative charge on the attacked atom is significantly connected with its ability to donate electrons to the electrophile and nucleophilicity. N1 (−0.2), N2 (−0.2), and N4 (−0.2) all have very negative Hirshfeld charges on their nitrogen atoms in all the *M*-SCN complexes. The Hg atom in Hg-Complex, the copper atom in Cu-Complex, and the carbon and hydrogen atoms in Pb-Complex all have the most positive ESP charges. It indicates they are essential biological targets through hydrogen bonding with the target. These atoms are also expected to be favourable sites for nucleophilic attack. The most electrophilic sites were sulphur and nitrogen, with the most negative portions of Hg-Complex and Cu-Complex. The examined molecule's component atoms' Mulliken charge values are detailed in Table S4.

9.4. ADME/T study

The exciting results were obtained from the ADME/T prediction utilizing the SwissADME server for *M*-SCN complexes. The compound's physiochemical characteristics, including its number of heavy atoms, hydrogen bond acceptors, donors, molar refractivity, topological polar surface area (TPSA), lipophilicity of the molecule, water solubility properties, high gastrointestinal absorption (GI), blood-brain barrier, skin permeation kinetics, and drug-likeness factors were calculated and shown in Table 4. Gastrointestinal absorption is found to be low for all the complexes. All three complexes tested negative for the CYP2D6 Inhibitor, demonstrating that there won't be any harmful side effects from the consumption of the drugs. Hg-Complex complies with Lipinski's Rule of Five, which states that a structure should be smaller than 500 Da. Topological polar surface area (TPSA), which measures the total number of polar atoms on the surface, is within the standard range for complexes, indicating reduced BBB permeability and, thus, a reduction in brain-related adverse effects. Additional elements are discussed in (Table 4).

- MW- Molecular Weight
- Fraction Csp3-the ratio of sp^3 hybridizes carbons over the total carbon count of the molecule.
- TPSA-topological polar surface area

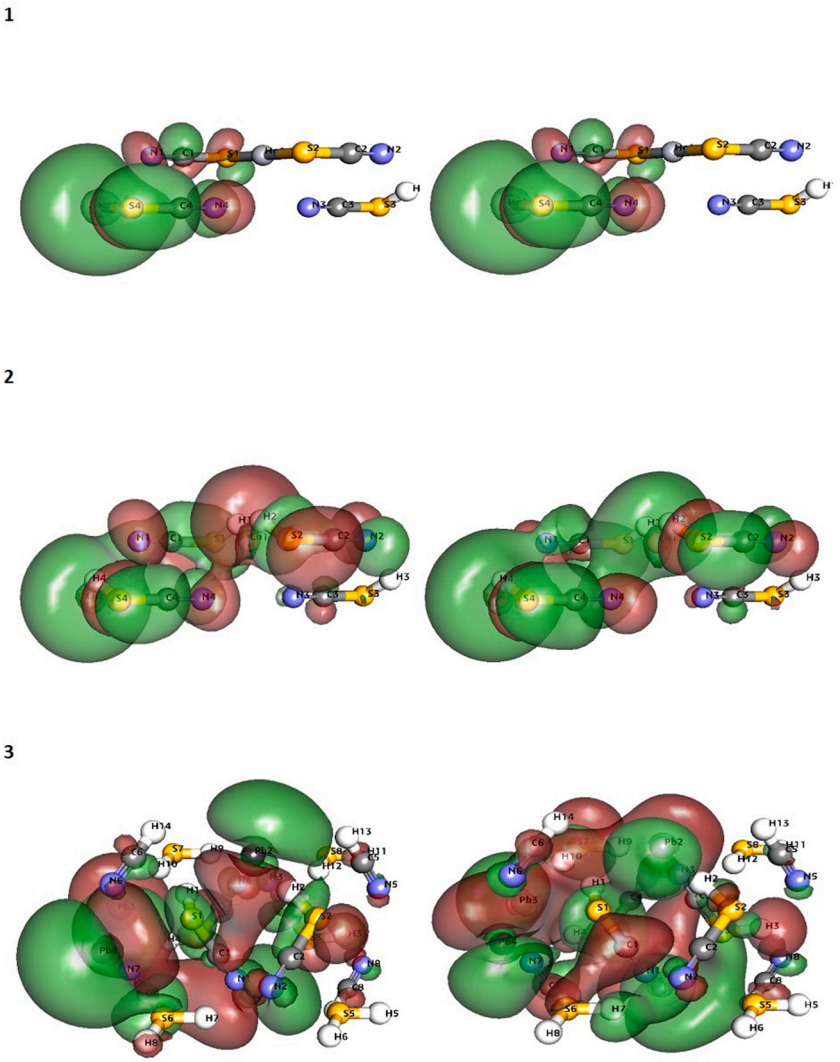

Fig. 5. Profiles for HOMO (Left) and LUMO (right) of Hg-complex (**1**), Cu-complex (**2**), and Pb-complex (**2**).

- log $P_{o/w}$ - partition coefficient between *n*-octanol and water
- XLOGP3, an atomistic method including corrective factors and a knowledge-based library [62].
- WLOGP, our own implementation of a purely atomistic method based on the fragmental system of Wildman and Crippen [63].
- MLOGP, an archetype of a topological method relying on a linear relationship with 13 molecular descriptors implemented from refs [64–66].
- SILICOS-IT, and hybrid method relying on 27 fragments and 7 topological descriptors.
- BBB -the blood-brain barrier
- *P*-gp - permeability glycoprotein
- CYP - cytochromes P450

9.5. Toxicity predictions

Discovery Studio 2.5 software was used to calculate the standard levels of ADME/T descriptors and toxicity predictions. The estimated ADME/T properties of the synthesized compounds are partially shown in Table 5, but details are given in Table S5. These complexes were also discovered to be aerobically non-degradable and passed tests for mutagenicity, skin sensitivity, and eye irritation. Here it explores that they all possess the desired characteristics to function as medications. Human Intestinal Absorption and Blood Brain Barrier (BBB) Using ADME/T PSA 2D and ADME/T A logp98 Properties (HIA). There are methods for getting non-penetrating medicines into the brain [67]. The three compounds were non-mutagenic. Additionally, compared to other compounds, they were expected to have lower Ame's mutagenicity and rodent carcinogenicity. Also, developmental toxicity potential powerfully highlights

Table 2
Global chemical reactivity parameters.

Name	Total Energy	Binding Energy	HOMO Energy eV	LUMO Energy eV	Dipole Moment	Band Gap Energy eV	Hardness	Softness	Electronegativity	Electrophilicity
Hg-Complex	−38764.61892413	−2.35196770	−0.14804723	−0.14777948	1.30289503	0.00026775	0.000133875	7469.654528478058	0.147913355	81.7118976185098
Cu-Complex	−5233.22910786	−2.44612815	−0.14124649	−0.13782125	0.50557846	0.00342524	0.00171262	583.9006901706158	0.13953387	5.684185889799518
Pb-Complex	−81996.06579037	−5.88319744	−0.11678102	−0.11283942	3.30204045	0.00394159	0.001970795	507.4094464416644	0.11481022	0.3839460464785784

Table 3
MESP iso-values and color scale.

Complex	Iso-value	Spectrum (Color range)		Histogram Scale
		Min	Max	
Pb-Complex	3.000000e-02	0.0000	4943.508	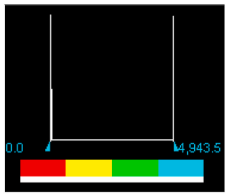
Cu-Complex	3.000000e-02	0.0000	709.2281	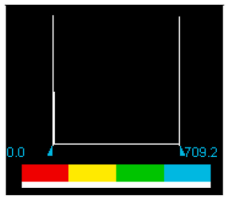
Hg-Complex	3.000000e-02	0.0000	2088.218	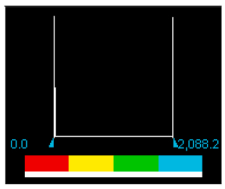

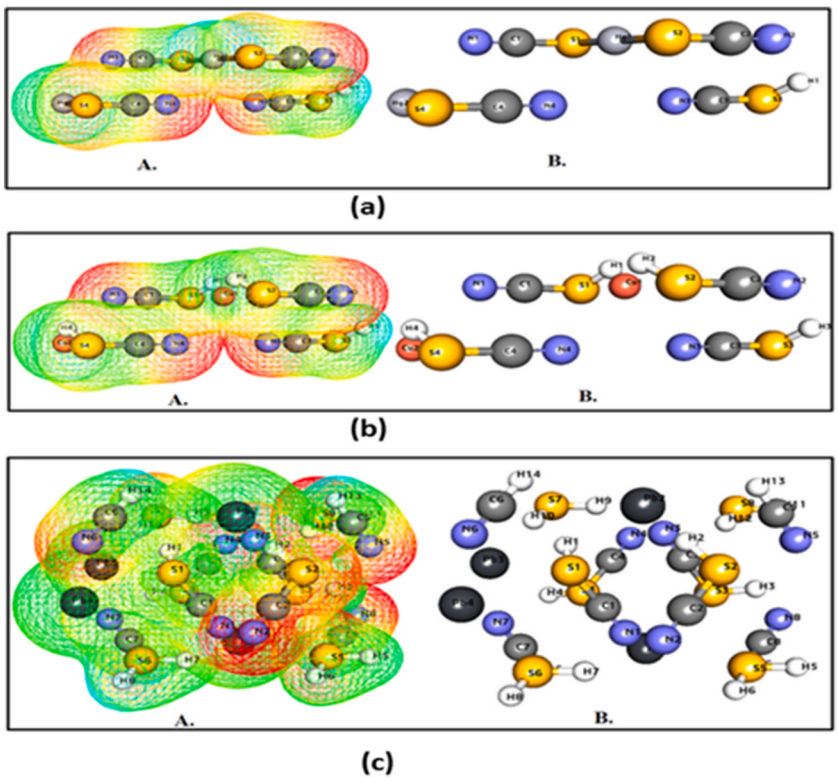

Fig. 6. Profiles (a–c) for 3D MESP of Hg-complex, Cu-complex, and Pb-complex.

Table 4
The calculated ADME/T parameters.

Parameters	Hg-Complex	Cu-Complex	Pb-Complex
Physicochemical Property			
Formula	$C_2HgN_2S_2$	$C_2CuN_2S_2$	$C_2PbN_2S_2$
Formula weight	316.75	179.71	323.36
Num. Heavy Atoms (Software generated)	14	14	28
Fraction Csp3	0.00	1.00	0.00
Num. Of Rotatable Bonds	2	5	0
Num. H-Bond Acceptors	4	4	8
Num. H-Bond Donors	0	4	0
Molar Refractivity	54.21	66.04	158.51
TPSA (A^2)	209.86	218.78	446.72
Lipophilicity			
Log $P_{o/W}$ (Ilogp)	0.00	0.00	0.00
Log $P_{o/W}$ (XLOGP3)	3.30	10.47	8.72
Log $P_{o/W}$ (WLOGP)	2.39	10.04	9.25
Log $P_{o/W}$ (MLOGP)	0.81	1.68	1.62
Log Po/W (SILICOS-IT)	0.43	−1.41	−1.38
Consensus Log $P_{o/W}$	1.39	416	3.64
Water Solubility			
Log S (ESOL) Solubility Class	−5.72, Moderately Soluble	−11.84, Insoluble	−10.07, Insoluble
Log S (ALI) Solubility Class	−7.38, Poorly Soluble	−13.97, Insoluble	−11.82, Insoluble
Log S (SILICO-IT) Solubility Class	−0.95, soluble	−12.67, Insoluble	−12.68, Insoluble
Pharmacokinetics			
GI Absorption	Low	Low	Low
BBB Permeation	No	No	No
P-Gp Substrate	No	Yes	No
CYP1A2 Inhibitor	No	No	No
CYP2C19 Inhibitor	Yes	No	No
CYP2C9 Inhibitor	No	No	No
CYP2D6 Inhibitor	No	No	No
CYP3A4 Inhibitor	No	Yes	Yes
Log K_p (Skin Permeation)	−7.83 cm/s	−4.28 C m/S	−4.79 C m/S
Drug Likeness			
Violation Of Lipinski's Rule of Five	yes	No	No
Ghose	No	No	No
Violation Of Veber Rule	No	No	No
Egan	NO	NO	NO
Muegge	NO	No	No
Bioavailability Score	0.55	0.55	0.55
Medicinal Chemistry			
Lead likeness	NO	NO	NO
Synthetic Accessibility	2.51	3.35	3.39

their potential use in therapeutic development.

9.6. Molecular docking

The binding site of Bacillus subtilis is almost filled by the compound Hg-Complex, which has an estimated binding energy of −97.152 kcal/mol. It formed a network of potent conventional hydrogen bonds with the residues Ile221, Leu249, UNKO, and Val245 (Fig.S3a/Table S6). Pi-Sulphur interactions involve specific cluster residues, such as Phe238. The complex is further strengthened by four metallic contacts between Hg and N and S. The complex becomes more stable through other interactions. The molecule Cu-Complex, which has an estimated binding energy of −94.108 kcal/mol, fills practically the entire binding site of Bacillus subtilis. It created a typical conventional hydrogen bond with the Thr247 residue (Fig.S3b/Table S6). A residue, such as Phe234, is involved in Pi-Sulphur interactions. The complex is further reinforced by creating two metallic connections between Cu–S and Cu–N. Other interactions make the complex more stable. With estimated binding energy of −97.140 kcal/mol, the molecule Pb-Complex virtually covers the complete binding site of Bacillus subtilis. It formed a conventional H-bond with important residues like Glu185, Arg215, Ser259, and Asn223 (Fig.S3c/Table S6). Additionally, it interacts with His267 and Ile268, pi-alkyl, and alkyl. The complex is strengthened by adding four metallic links between Pb–S and Pb–N. The complex is more stable due to other interactions. The binding site of Proteus Vulgaris is almost filled by the compound Hg-Complex, which has an estimated binding energy of −112.661 kcal/mol. It formed a network of potent conventional hydrogen bonds with the residues Gln99, Tyr97, and Gln280 (Figure S4a/Table S6). The complex is further strengthened by four metallic contacts between Hg, N, and S. The complex becomes more stable through other interactions. The Cu-Complex, which has an estimated binding energy of −112.41 kcal/mol, fills practically the entire binding site of Proteus Vulgaris. The residues Leu262, Tyr277, Gly357, Gln350, and Asn353 created a network of strong conventional hydrogen bonds (Figure S4b/Table S6). The complex is further reinforced by creating four metallic connections between Hg–N and Hg–S. Other interactions make the complex more stable. The molecule Pb-Complex, with an estimated binding energy of −112.283 kcal/mol,

Table 5
Toxicity predictions.

Parameters	Hg-Complex	Cu-Complex	Pb-Complex
ADMET Solubility	−1.261	−0.457	−0.457
ADMET Solubility level	4	4	4
ADMET unknown AlogP98	1	0	0
ADMET BBB	−0.431	−0.317	−0.317
ADMET BBB level	2	2	2
ADMET-EXT-CYP2D6	−2.74484	−3.61964	−4.72823
ADMET-EXT-CYP2D6#prediction	False	False	False
ADMET-EXT-CYP2D6-Applicability	−3.3847		
ADMET-EXT-CYP2D6-Applicability#MD	20.4291	14.261	32.2821
ADMET-EXT-CYP2D6-Applicability#MDpvalue	1.15251e-12	1.36518e-05	1.16262e-24
ADMET-EXT- Hepatotoxic	0.135619	0.0912133	1.41364
ADMET-EXT- Hepatotoxic #prediction	True	True	True
ADMET-EXT- Hepatotoxic Applicability	Within expected range	Within expected range	Within expected range
ADMET-EXT- Hepatotoxic Applicability #MD	13.2927	9.31101	22.6407
ADMET-EXT- Hepatotoxic Applicability #MDpvalue	4.22711e-07	0.30867	2.38248e-35
ADMET Absorption level	0	0	0
ADMET-EXT-PPB	−3.973	−4.07027	−5.27727
ADMET-EXT-PPB #Prediction	False	False	False
ADMET-EXT-PPB- Applicability	Within expected range	Within expected range	Within expected range
ADMET-EXT-PPB- Applicability #MD	15.5492	14.2618	27.4791
ADMET-EXT-PPB- Applicability #MDpvalue	2.76353e-08	3.06969e-05	2.30912e-57
ADMET-AlogP98	1.45	0.645	0.645
ADMET-PSA-2D	45.87	22.935	22.935

almost completely covers the whole binding site of Bacillus subtilis. It made a predicted conventional hydrogen connection with the residues Gln99, Glu140, and Asp340 (Fig.S4c/Table S6). Residues like Phe301 and Phe341 are essential in interactions with pi-sulphur. It results in pi-alkyl and alkyl interactions between Trp438 and Arg315, Pro342, and Lys104. The addition of four metallic connections enhances Pb–S and Pb–N. Due to other interactions, the complex is more stable.

10. Antibacterial portal

10.1. Mean zone diameter

To test for antimicrobial potency, we measured the zone diameter of Hg-Complex, Pb-Complex, and Cu-Complex complexes, as well as common metal salts such as $HgCl_2$, NaSCN, $Cu(NO_3)_2$, and $Pb(NO_3)_2$, against two gm-positive and two gm-negative bacterial strains (Fig.S5). We also analyzed the same activity for the standard metal salts since they are used in complex preparation. The mean values of the zone diameter for all the tested compounds are accurately recorded in Table 6. The compounds were active against all the selected microbes except NaSCN against *Pseudomonas aeruginosa* and *Escherichia coli.* In this study, the compounds showed similar activity against the chosen microbes. The Hg-Complex was the most reactive against *Escherichia coli,* followed by *Pseudomonas aeruginosa* and *Staphylococcus aureus*, and *Bacillus subtilis* is the least reactive. For the compound, Pb-Complex and Cu-Complex, the order of reactivity were *Bacillus subtilis* > *Escherichia coli* > Pseudomonas *aeruginosa* ≈ *Staphylococcus aureus*. In the case of $HgCl_2$, Pseudomonas *aeruginosa* > *Bacillus subtilis* > *Escherichia coli* > *Staphylococcus aureus*. For NaSCN, the order *Staphylococcus aureus* ≈ *Bacillus subtilis* but no reactivity against *Escherichia coli* and *Pseudomonas aeruginosa*. Reactivity of $Cu(NO_3)_2$, was *Escherichia coli* > *Bacillus subtilis* > *Staphylococcus aureus* > *Pseudomonas aeruginosa*, and $Pb(NO_3)_2$ *Pseudomonas aeruginosa* > *Escherichia coli* > *Bacillus subtilis* ≈ *Staphylococcus aureus*. Of the compounds tested, Hg-Complex and HgCl2 had the most substantial antimicrobial effects against all the selected microbes. On the other hand, $Pb(NO_3)_2$ and Cu-Complex showed less activity. Pb-Complex and metal salts, $Cu(NO_3)_2$ and NaSCN had similar effects to each other and were effective against *Escherichia coli, Bacillus subtilis, Staphylococcus aureus, and Pseudomonas aeruginosa.*

10.2. The MIC calculations

This study aimed to determine the minimum inhibitory concentration of compounds with good antibacterial activity. The activity of synthesized compounds against pathogens varied, possibly due to differences in bacterial structure features. Gram-negative bacteria have an impermeable outer layer on top of peptidoglycan. In contrast, Gram-positive bacteria have a negatively charged polysaccharide, tachyonic acid, in their outer cell wall, which helps positively charged ions penetrate the cell. As a result, the complexes showed high antibacterial activity. Table 7 summarizes all the MIC results, revealing that the compounds had a value of 6.25 μg mL^{-1} against all selected microbes. MIC data indicated that the structural changes in ligands improved their potency as antibacterial agents.

Table 6
Mean zone diameter for the compounds and metal salts.

Fungal strain/sample	Hg-Complex	Zone of inhibition ± standard deviation (mm)					
		Pb-Complex	Cu-Complex	$HgCl_2$	NaSCN	$Cu(NO_3)_2$	$Pb(NO_3)_2$
S. aureus	5.20 ± 1.67	1.50 ± 1.04	3.10 ± 0.83	5.00 ± 0.74	1.20 ± 0.44	1.60 ± 0.79	3.50 ± 1.37
B. subtilis	5.00 ± 0.72	1.80 ± 0.19	4.30 ± 1.57	5.50 ± 2.81	1.20 ± 1.42	1.80 ± 0.58	3.50 ± 1.73
P. aeruginosa	5.20 ± 0.98	1.50 ± 1.96	3.10 ± 0.31	5.80 ± 0.27	–	1.30 ± 0.92	4.00 ± 0.88
E. coli	5.80 ± 1.23	1.60 ± 1.45	3.60 ± 1.34	5.30 ± 0.22	–	2.00 ± 1.83	3.90 ± 0.54

Each value represents six replications' mean ± standard deviation (SD). –: not detected inhibition.

Table 7
Minimum Inhibitory Concentration (μg/mL) values of compounds Hg-Complex and $HgCl_2$ against pathogens strains based on the Agar Dilution Method.

Microorganism/sample	MIC (μg/mL)			
	Gram-positive bacteria		Gram-negative bacteria	
	S. aureus	B. subtilis	*P. aeruginosa*	*E. coli*
Hg-Complex	6.25	6.25	6.25	6.25
$HgCl_2$	6.25	6.25	6.25	6.25

10.3. The time-kill kinetics

The time-kill kinetic study provides essential information about how the synthesized compound interacts with microorganisms and affects their growth. This study shows promise for using the compound to treat diseases caused by these bacteria. The results of the time-kill kinetics study for the sample (Hg-Complex) against all microorganisms can be seen in Fig. S6. As shown in Fig. S6, the untreated controls in each case represented the standard growth curve against *Staphylococcus aureus, Bacillus subtilis, Pseudomonas aeruginosa*, and *Escherichia coli*. Where the lag period remained for 1 h, the exponential growth or the log phase occurred, followed by a stationary phase. In the case of Hg-Complex for the microorganisms, a very short exponential growth phase was observed compared to the untreated control. The growth inhibition was observed at 4–8 h of the incubation period; around the 8th hour of incubation, the bacterial CFU enters the declining phase, i.e., the death phase, except for *S. aureus*, which penetrates the death phase around the 4th h. Thus, this observation revealed that compound Hg-Complex shows promising bactericidal activities, especially against *S. aureus*.

11. Conclusions

The article flourishingly synthesized Hg/Cu/Pb–SCN crystal compounds with satisfactory yields. Modern spectroscopic tools and *S*C-XRD characterized the compounds. EDX-SEM has examined the elemental composition and size morphology. In gas phase B3LYP-D3/6-311G (d, p) level, DFT calculations optimized the compound's molecular geometry. DFT explored global reactivity, HOMO-LUMO parameters, atomic properties, and MESP to ensure chemical reactivity. The complexes' crystal packing comprises weak covalent bonding and Pb…S contacts known as tetrel bonding. Hirshfeld surface and 2D fingerprint plots divulge the supramolecular interactions. An in-depth article demonstrated *in silico* molecular docking against the Gm + ve Bacillus subtilis (6UF6) and Gm -ve Proteus Vulgaris to support the bactericidal activity of the synthesized compounds. In addition, antibacterial activity with MIC (g/mL) values and time-kill kinetics were performed against *Staphylococcus aureus* (ATCC 25923) and *Bacillus subtilis* (ATCC 6635) as gram-positive bacteria and *Pseudomonas aeruginosa* (ATCC 27853) and *Escherichia coli* (ATCC 25922) as gram-negative bacteria. ADME/T has established the theoretical drug-like properties examined in detail using the SWISSADME database. ADME/T estimated the lipophilicity of the molecule, consensus P0/W, and water solubility properties. Finally, the perspective of the research study is that synthesized compounds are used today as promising drugs and antimicrobial agents.

Author contribution statement

DHRUBA JYOTI MAJUMDAR: Conceived and designed the experiments; Performed the experiments; Analyzed and interpreted the data; Contributed reagents, materials, analysis tools or data; Wrote the paper.

Jessica Elizabeth Philip: Performed the experiments; Wrote the paper.

Amit Dubey, Aisha Tufail: Performed the experiments; Analyzed and interpreted the data; analysis tools or data, Wrote the paper.

SOURAV ROY: Analyzed and interpreted the data; Wrote the paper.

Data availability statement

The data that has been used is confidential.

Declaration of competing interest

The authors declare no competing interest or personal relationships that could have appeared to impact the work reported in this article.

Acknowledgments

The current research has not explicitly been funded by any public, commercial or not-for-profit sectors. All authors of the manuscript carefully read and approved the final version before submission.

Appendix B. Supplementary data

Supplementary data to this article can be found online at https://doi.org/10.1016/j.heliyon.2023.e16103.

Appendix A. Supplementary material

CCDC 2205318–2205320 contains the supplementary full crystallographic data for the complexes. These data can be obtained free of charge via http://www.ccdc.cam.ac.uk/conts/retrieving.html, or from the Cambridge Crystallographic Data Center, 12 Union Road, Cambridge CB2 1EZ, UK; fax: (+44) 1223-336-033; or e-mail: deposit@ccdc.cam.ac.uk.

References

[1] P. Bhowmik, S. Chattopadhyay, M.G.B. Drew, C. Diaz, A. Ghosh, Synthesis, structure and magnetic properties of mono- and di-nuclear nickel(II) thiocyanate complexes with tridentate N_3 donor Schiff bases, Polyhedron 29 (2010) 2637–2642.
[2] M. Monfort, J. Ribas, X. Solans, M. Monfort, J. Ribas, X. Solans, Crystal structures and ferromagnetic properties of two new dinuclear complexes with thiocyanato bridging ligands:{[Ni_2(1,2-diamino-2-methylpropane)$_3$(NCS)$_2$]$_2$(mu.-NCS)$_2$}[Ni(1,2-diamino-2 methylpropane)$_2$(NCS)$_2$].cntdot.H_2O and [{Ni_2(1,2-diamino-2-methylpropane)$_4$}(mu.-NCS)$_2$](PF6)$_2$, magneto-structural correlations, Inorg. Chem. 33 (1994) 4271–4276.
[3] J. Ribas, A. Escuer, M. Monfort, R. Vicente, R. Cortes, L. Lezama, T. Rojo, Polynuclear NiII and MnII azido bridging complexes: structural trends and magnetic behavior, Coord. Chem. Rev. 193–195 (1999) 1027–1068.
[4] P. Orioli, B. Bruni, M.D. Vaira, L. Messori, F. Piccioli, Decomposition of ascorbic acid in the presence of cadmium ions leads to formation of a polymeric cadmium oxalate species with peculiar structural features, Inorg. Chem. 41 (2002) 4312–4314.
[5] H.D. Bian, W. Gu, J.-Y. Xu, F. Bian, S.-P. Yan, D.-Z. Liao, Z.-H. Jiang, P. Cheng, The first μ3-oxalato-bridged copper complex with tridentate schiff base ligand N-ethyl-N'-Salicylidene-1,2-diaminoethane: synthesis, structure, and magnetic properties, Inorg. Chem. 42 (2003) 4265–4267.
[6] A.H. Norbury, A.I.P. Sinha, The co-ordination of ambidentate ligands, Q. Rev. Chem. Soc. 24 (1970) 69–94.
[7] S. Paul, R. Clerac, N.G.R. Hearns, D. Ray, Novel layering of aqua and imidazolidinyl phenolate bridged cationic $[Cu^{II}_2(\mu\text{-}L)(\mu\text{-}H_2O)\cdot H_2O]_2$ Units over $Cu^{I}NCS$ based one-dimensional anionic parallel chains as diamagnetic coordination framework host, Cryst. Growth Des. 9 (2009) 4032–4040.
[8] D.J. Majumdar, S. Roy, A. Frontera, The importance of tetrel bonding interactions with carbon in two arrestive iso-structural Cd(ii)–Salen coordination complexes: a comprehensive DFT overview in crystal engineering, RSC Adv. 12 (2022) 35860–35872.
[9] D.J. Majumdar, B. Tüzün, T.K. Pal, S. Das, K.P. Bankura, Architectural view of flexible aliphatic–OH group coordinated hemi-directed Pb(II)-Salen coordination polymer: synthesis, crystal structure, spectroscopic insights, supramolecular topographies, and DFT perspective, J. Inorg. Organomet. Polym. 32 (2022) 1159–1176.
[10] D.J. Majumdar, A. Frontera, Rosa M. Gomila, S. Das, K.P. Bankura, Synthesis, spectroscopic findings and crystal engineering of Pb(II)–Salen coordination polymers, and supramolecular architectures engineered by σ-hole/spodium/tetrel bonds: a combined experimental and theoretical investigation, RSC Adv. 12 (2022) 6352–6363.
[11] D.J. Majumdar, S. Dey, D. Das, D.K. Singh, S. Das, K.P. Bankura, D. Mishra, Heterometallic Zn(II)-K(I) complex with Salen-type Schiff-base ligand: synthesis, crystal structure, solid-state photoluminescent property and theoretical study, J. Mol. Struct. 1185 (2019) 112–120.
[12] H.A. Yassa, Autism: a form of lead and mercury toxicity, Environ. Toxicol. Pharmacol. 38 (3) (2014) 1016–1024.
[13] J.H. Mohammadabadi, A. Rahmatian, F. Sayehmiri, M. Rafiei, Mohammad, The relationship between the level of copper, lead, mercury and autism disorders: a meta-analysis, Pediatr. Health Med. Therapeut. 11 (2020) 369–378.
[14] H. G-Maladonado, O. P-Lopez, C.G. Billiaderis, Amylolytic enzymes and products derived from starch: a review, Crit. Rev. Food Sci. Nutr. 35 (5) (1995) 373–403.
[15] A.J. P-Fonseca, J. C-Rosas, C.A. G-Aldapa, T. T-Benitez, B.M. Millan-Malo, A.D. Real, Effect of the alkaline and acid treatments on the physicochemical properties of corn starch, J. Foodserv. 11 (2002) 67–74.
[16] M.D. Johnson, E. Larry E (Eds.), "Copper". Merck Manual Home Health Handbook, Merck Sharp & Dohme Corp., a subsidiary of Merck & Co., Inc., 2008.
[17] E.S. Claudio, H.A. Godwin, J.S. Magyar, Fundamental coordination chemistry, environmental chemistry, and biochemistry of lead(II), John Wiley & Sons, Inc. 51 (2002) 1–144.
[18] M. Maiti, B. Kundu, S.C. Kundu, D. Ray, Copper(II) complexes of piperazine based ligand: synthesis, crystal structure, protein binding and evaluation of anti-cancerous therapeutic potential, Inorg. Chim. Acta. 418 (2014) 30–41.
[19] D.J. Majumdar, T.K. Pal, S.A. Shakib, S. Das, K.P. Bankura, D. Mishra, Synthesis, spectroscopic characterization, and SC-XRD study of one privileged heteronuclear Ni(II)/Hg(II)-Salen complex: an exclusive DFT outlook, Inorg. Chem. Commun. 128 (2021), 108609.
[20] A.L. Beaucham, D. Goutier, Structure cristalline et molCculaire do thiocyanate mercurique, Can. J. Chem. 50 (1972) 977–981.
[21] J.A.A. Mokuolu, J.C. Speakman, The crystal structure of lead thiocyanate, Chem. Commun. (1966) 25.
[22] M. Kabesova, M. Dunajjurco, M. Serator, J. Gazo, The crystal structure of copper(I) thiocyanate and its relation to the crystal structure of copper(I1), Diammine Dithiocyanate Complex 17 (1976) 161–165.
[23] M.A.A.H. Allah, A.A. Balakit, H.E. Salman, A.A. Abdulridha, Y. Sert, New heterocyclic compound as carbon steel corrosion inhibitor in 1 M H_2SO_4, high efficiency at low concentration: experimental and theoretical studies, J. Adhes. Sci. Technol. 37 (2023) 525–547.
[24] A.A. Abdulridha, M.A.A.H. Allah, S.Q. Makki, Y. Sert, H.E. Salman, A.A. Balakit, Corrosion inhibition of carbon steel in 1 M H_2SO_4 using new Azo Schiff compound: electrochemical, gravimetric, adsorption, surface and DFT studies, J. Mol. Liq. 315 (2020), 113690.
[25] A.A. Balakit, S.Q. Makki, Y. Sert, F. Ucun, M.B. Alshammari, P. Thordarson, G.A. Ei-Hiti, Synthesis, spectrophotometric and DFT studies of new Triazole Schiff bases as selective naked-eye sensors for acetate anion, J. Adhes. Sci. Technol. 32 (2020) 519–526.

[26] N. Degi, H. Gokce, O.E. Dogan, G. Alpasnan, T. Agar, S. Muthu, Y. Sert, Quantum computational, spectroscopic investigations on N-(2-((2-chloro-4,5-dicyanophenyl) amino)ethyl)-4-methylbenzenesulfonamide by DFT/TD-DFT with different solvents, molecular docking and drug-likeness researches, Colloids and Surf. Physicochem. Engin. Aspects 638 (2022), 128311.
[27] C. Alasalvar, N. Ozturk, A.A.-M. Abdel-Aziz, H. Gokce, A.S. Ei-Azad, Y. Sert, Molecular structure, Hirshfeld surface analysis, spectroscopic (FT-IR, Laser-Raman, UV–vis. and NMR), HOMO-LUMO and NBO investigations on *N*-(12-amino-9,10-dihydro-9,10-ethanoanthracen-11-yl)-4-methylbenzenesulfonamide, J. Mol. Struct. 1171 (2018) 696–705.
[28] L. Guan, H. Yang, Y. Cai, L. Sun, P. Di, W. Li, G. Liu, Y. Tang, ADMET score-A comprehensive scoring function for evaluation of chemical drug-likeness, Med. Chem. Commun. 10 (2019) 148–157.
[29] M. Toscano, N. Russo, Soybean aglycones antioxidant activity. A theoretical investigation, Comput. Theor. Chem. 1077 (2016) 119–124.
[30] M. Leopoldini, I. Prieto Pitarch, N. Russo, M. Toscano, Structure, conformation, and electronic properties of apigenin, luteolin, and taxifolin antioxidants. A first principle theoretical study, J. Phys. Chem. B 108 (2004) 92–96.
[31] M. Leopoldini, N. Russo, M. Toscano, Antioxidant properties of phenolic compounds: H-atom versus electron transfer mechanism, J. Phys. Chem. A 108 (2004) 4916–4922.
[32] G. Mazzone, N. Malaj, A. Galano, N. Russo, M. Toscano, Antioxidant properties of several coumarin–chalcone hybrids from theoretical insights, RSC Adv. 5 (2015) 565–575.
[33] M. Leopoldini, T. Marino, N. Russo, M. Toscano, Density functional computations of the energetic and spectroscopic parameters of quercetin and its radicals in the gas phase and in solvent, Theor. Chem. Acc. 111 (2004) 210–216.
[34] M.J. Frisch, G.W. Trucks, H.B. Schlegel, G.E. Scuseria, M.A. Robb, J.R. Cheeseman, G. Scalmani, V. Barone, B. Mennucci, G.A. Petersson, et al., Gaussian 09, Revision E.01, Gaussian Inc., Wallingford, CT, USA, 2016.
[35] M.A. Spackman, D. Jayatilaka, Hirshfeld surface analysis, CrystEngComm 11 (2009) 19–32.
[36] F.L. Hirshfeld, Bonded-atom fragments for describing molecular charge densities, Theor. Chem. Acta. 44 (1977) 129–135.
[37] H.F. Clausen, M.S. Chevallier, M.A. Spackman, B.B. Iversen, Three new co-crystals of hydroquinone: crystal structures and Hirshfeld surface analysis of intermolecular interactions, New J. Chem. 34 (2010) 193–199.
[38] A.L. Rohi, M. Moret, W. Kaminsky, K. Claborn, J.J. McKinnon, B. Kahr, Hirshfeld surfaces identify inadequacies in computations of intermolecular interactions in crystals: pentamorphic 1,8-dihydroxyanthraquinone, Cryst. Growth Des. 8 (2008) 4517–4525.
[39] A. Parkin, G. Barr, W. Dong, C.J. Gilmore, D. Jayatilaka, J.J. McKinnon, M.A. Spackman, C.C. Wilson, Comparing entire crystal structures: structural genetic fingerprinting, CrystEngComm 9 (2007) 648–652.
[40] M.A. Spackman, J.J. McKinnon, Fingerprinting intermolecular interactions in molecular crystals, CrystEngComm 4 (2002) 378–392.
[41] B.R. Chandrika, J. Subramanian, S.D. Sharma, Managing protein flexibility in docking and its applications, Drug Discov. Today 14 (2009) 394–400.
[42] J.D. Durrant, J.A. McCammon, Computer-aided drug-discovery techniques that account for receptor flexibility, Curr. Opin. Pharmacol. 10 (2010) 770–774.
[43] F.K.K. Li, F.I. Rosell, R.T. Gale, J.P. Simorre, E.D. Brown, N.C.J. Strynadka, Crystallographic analysis of *Staphylococcus aureus*LcpA, the primary wall teichoic acid ligase, J. Biol. Chem. 295 (9) (2020) 2629–2639.
[44] Y. Ju, S. Tong, Y. Gao, W. Zhao, Q. Liu, Q. Gu, J. Xu, L. Niu, M. Teng, H. Zhou, Crystal structure of a membrane-bound l-amino acid deaminase from Proteus vulgaris, J. Struct. Biol. 195 (3) (2016) 306–315.
[45] A. Dubey, A. Marabotti, P.W. Ramteke, A. Facchiano, *In silico* approach to find chymase inhibitors among biogenic compounds, Future Med. Chem. 8 (2016) 841–851.
[46] A. Dubey, A. Marabotti, P.W. Ramteke, A. Facchiano, Interaction of human chymase with ginkgolides, terpene trilactones of Ginkgo biloba investigated by molecular docking simulations, Biochem. Biophys. Res. Commun. 473 (2016) 449–454.
[47] S. Bharadwaj, A. Dubey N.K. Kamboj, A.K. Sahoo, S.G. Kang, U. Yadava, Drug repurposing for ligand-induced rearrangement of Sirt2 active site-based inhibitors via molecular modeling and quantum mechanics calculations, Sci. Rep. 11 (1) (2021), 10169.
[48] A. Dubey, S. Dotolo, P.W. Ramteke, A. Facchiano, A. Marabotti, Searching for chymase inhibitors among chamomile compounds using a computational-based approach, Biomolecules 9 (1) (2018) 5.
[49] ChemBioDraw Ultra (version 12.0.2.1076), 1986ñ2010 CambridgeSoft, ChemBio3D Ultra (Version 12.0.2.1076), 1986ñ2010 CambridgeSoft, Molegro Virtual Docker, CLC Bio-2012, version 5.5.
[50] A. Daina, O. Michielin, V. Zoete, SwissADME: a free web tool to evaluate pharmacokinetics, drug-likeness and medicinal chemistry friendliness of small molecules, Sci. Rep. 7 (2017), 42717.
[51] A. Lapasam, V. Banothu, U. Addepally, M.R. Kollipara, Synthesis, structural and antimicrobial studies of half-sandwich ruthenium, rhodium and iridium complexes containing nitrogen donor Schiff-base ligands, J. Mol. Struct. 1191 (2019) 314–322.
[52] H. Kargar, M. Fallah-Mehrjardi, R. Behjatmanesh-Ardakani, H.A. Rudbari, A.A. Ardakani, S. Sedighi-Khavidak, K.S. Munawar, M. Ashfaq, M.N. Tahir, Binuclear Zn(II) Schiff base complexes: synthesis, spectral characterization, theoretical studies and antimicrobial investigations, Inorg. Chim. Acta. 530 (2022), 120677.
[53] D. Baecker, Ö. Sesli, L. Knabl, S. Huber, D. Orth-Höller, R. Gust, Investigating the antibacterial activity of salen/salophene metal complexes: induction of ferroptosis as part of the mode of action, Eur. J. Med. Chem. 209 (2021), 112907.
[54] G.M. Sheldrick, SADABS, a Software for Empirical Absorption Correction, Ver.2.05, University of Göttingen: Göttingen, Germany, 2002.
[55] SMART & SAINT Software Reference Manuals Version 6.45, Bruker Analytical X-ray Systems, Inc., Madison, WI, 2003.
[56] SHELXTL Reference Manual Ver. 6.1, Bruker Analytical X-ray Systems, Inc., Madison, WI, 2000.
[57] G.M. Sheldrick, SHELXTL, a Software for Empirical Absorption Correction Ver.6.12, Bruker AXS Inc.: WI. Madison, 2001.
[58] O.V. Dolomanov, L.J. Bourhis, R.J. Gildea, J.A.K. Howard, H. Puschmann, OLEX2, OLEX2: a complete structure solution, refinement, and analysis program, J. Appl. Crystallogr. 42 (2009) 339–341.
[59] S. Roy, M.G.B. Drew, A. Bauzá, A. Frontera, S. Chattopadhyay, Non-covalent tetrel bonding interactions in hemidirectional Pb(II) complexes with nickel(ii)-salen type metalloligands, New J. Chem. 42 (2018) 6062–6076.
[60] D. Zeroka, J.O. Jensen, A.C. Samuels, Infrared spectra of some isotopomers of ethylamine and the ethylammonium ion: a theoretical study, J. Mol. Struct. 465 (1999) 119–139.
[61] A.O. Zacharias, A. Varghese, K.B. Akshaya, M.S. Savitha, L. George, DFT, spectroscopic studies, NBO, NLO and Fukui functional analysis of 1-(1-(2,4-difluorophenyl)-2-(1H-1,2,4-triazol-1-yl) ethylidene) thiosemicarbazide, J. Mol. Struct. 1158 (2018) 1–13.
[62] R.G. Pearson, Hard and soft acids and bases-the evolution of a chemical concept, Coord. Chem. Rev. 100 (1990) 403–425.
[63] T. Cheng, Computation of Octanol−Water partition coefficients by guiding an additive model with knowledge, J. Chem. Inf. Model. 47 (2007) 2140–2148.
[64] S.A. Wildman, G.M. Crippen, Prediction of physicochemical parameters by atomic contributions, J. Chem. Inf. Model. 39 (1999) 868–873.
[65] I. Moriguchi, H. Shuichi, Q. Liu, I. Nakagome, Y. Matsushita, Simple method of calculating octanol/water partition coefficient, Chem. Pharm. Bull. 40 (1992) 127–130.
[66] I. Moriguchi, H. Shuichi, I. Nakagome, H. Hirano, Comparison of reliability of log P values for Drugs calculated by several methods, Chem. Pharm. Bull. 42 (1994) 976–978.
[67] R. Gabathuler, approaches to transport therapeutic drugs across the blood-brain barrier to treat brain diseases, Neurobiol. Dis. 37 (2010) 48–57.